Transmission characteristics of multilayer metal polarization insensitive metasurface

GUANJUN FENG[1], CHEN WANG[2], YUMING LIN[3], MINGFENG ZHENG[4], MANNA GU[5,*], FUHAI LIU[6], YONG TAO[4], YANLING LI[7], YING TANG[2,8], YING TIAN[2]
[1]*Zhejiang Tongji Vocational College of Science and Technology, Hangzhou, 311231, China*
[2]*Institute of Optoelectronic Technology, China Jiliang University, Hangzhou 310018, China*
[3]*Hangzhou Xio Elevator Modernization Update Co., LTD, China*
[4]*Geely Automotive Institute, Hangzhou Vocational and Technical College, Hangzhou, 310018, China*
[5]*College of Information Engineering, China Jiliang University, Hangzhou 310018, China*
[6]*Special Equipment Institute, Hangzhou Vocational and Technical College, Hangzhou 310018, China*
[7]*Jiaxing Nanhu University, Jiaxing, China*
[8]*Nanhu Laboratory, Jiaxing, China*

A polarization insensitive encoding Huygens metasurface is proposed. A multilayer symmetric metal structure is proposed to construct a transmission-coded metasurface because the single-layer metal structure cannot realize the all-phase control of the unit structure. In order to optimize the design of the eight element structures with the abrupt phase interval of π/4 and high transmittance, three different structures of square, circular and circular metal patches were optimized to construct the unit structures. The phase of the periodic element structure was changed by changing the length of the square metal patch, the size of the inner and outer frame of the circular metal patch and the radius of the circular metal patch. Based on the S-parameter inversion algorithm, we calculated the effective impedance, dielectric constant and effective permeability of the three cell structures, which provides the physical mechanism basis for the interpretation of beam regulation of coded metasurface. In order to realize the beam control characteristics of Huygens coded metasurface, we first arrange the optimally designed unit structures into an ordered array structure. The near-field and far-field scattering characteristics of coded arrays are calculated by finite element method. In order to further realize the free regulation of far-field scattered beam, Fourier convolution principle in digital signal processing is introduced. Fourier convolution addition operation is carried out on two different coded metassurface sequences to realize the free regulation of scattered beam.

(Received December 11, 2024; accepted June 4, 2025)

Keywords: Scattering, Microstructure, Metamaterials, Surface

1. Introduction

Metasurface is a kind of artificial special material structure composed of sub-wavelength unit structure arranged in a certain order (1-8]. Because metasurface has electromagnetic field characteristics different from surfaces composed of other materials [9,20], it can adjust and control electromagnetic wave by changing the material, thickness, cycle length, arrangement sequence, number of structural layers and rotation angle of unit structure [21,30]. Compared with the surface composed of ordinary materials, the metasurface has smaller thickness, more variable shape, easy processing and low loss, low absorptivity for incident materials and easy integration of surface shape [31,40].

Huygens metasurface is an efficient artificial electromagnetic surface based on Huygens equivalence principle. Compared with other metasurfaces [41,56] the Huygens metasurface has better electromagnetic properties, because the Huygens metasurface contains both electric and magnetic resonators. By adjusting these two resonators, the Huygens metasurface can obtain different electromagnetic characteristics. Huygens metasurface, also known as the equivalent impedance surface, can manipulate the amplitude, phase and polarization of electromagnetic waves. Huygens metasurface is widely used in beam deflectors, vortex beams and polarization controllers. In 2014, the concepts such as "coded metasurface" and "programmable metasurface" were proposed successively [57]. By means of digital control, taking the most basic assembly language binary as an example, the unit structure corresponding to 0° phase can be regarded as "0" in binary, and the unit structure corresponding to 180° phase can be regarded as "1" in binary. Thus, the regulation of electromagnetic wave can be realized by digital method. Compared with traditional metasurface, digital coded metasurface control is flexible and easy to operate in electromagnetic wave field.

Here, we encode the Huygens metasurface unit structure to construct the coded Huygens metasurface. At

present, all-dielectric materials are generally used in the design process of most transmission-type metasurface element structures. However, all-dielectric material structures require the use of electron beam lithography. The unit structure of metal materials has certain advantages in the preparation process. However, it is difficult for single-layer metal structures to achieve 360° phase change. We propose a multi-layer metal structure that can achieve 360° phase change. The direction control of transmitted beam mainly applies the generalized Snell's law, but the direction control of beam transmission is limited, because the cell structure needs gradual arrangement. In order to realize the free control of transmitted beam, we introduce the Fourier convolution operation of coded Huygens metasurface.

Fourier coding convolution principle can realize continuous angular scanning by using finite number of state coding units [58,61]. Thanks to the Fourier transform relationship between the encoding pattern of the encoding metasurface and its far-field orientation pattern, they innovatively apply the convolution eigenvalue in signal processing to the regulation of the far-field orientation pattern, that is, by superimposed another gradient encoding sequence on the existing encoding pattern, the far-field radiation orientation pattern can be deflected towards a certain design direction. This operation of rotating the far-field pattern to a larger angle is similar to the process of moving the baseband signal to the high-frequency carrier by the Fourier transform. By superimposing different periodic coding patterns, the far-field pattern can be deflected to multiple directions almost lossless, showing the strong and flexible control ability of the designed coding scheme for electromagnetic waves.

2. Encoding Huygens metasurface unit structure

Usually, metasurface is studied from the physical level, such as surface dielectric constant, surface impedance, amplitude, phase and other parameters of metasurface to characterize the electromagnetic characteristics of the interface [62,79]. Recently, the concepts of digital coding metasurface, reconfigurable digital metasurface and information metasurface have been proposed. The sequence metasurface is formed by the arrangement of the phase discontinuous element structure, which can quickly change the reflection, transmission and scattering of the beam through the metasurface. Most of the current research focuses on 1-bit, 2-bit, and 3-bit coded metasurfaces. 1-bit is composed of two structures with phase differences of 180°, with "0" representing 0° and "1" representing 180°. 2-bit is a unit structure with four codes of "00", "01", "10" and "11" respectively representing four phase differences of 90°. The 3-bit is a structure consisting of eight codes "000", "001", "010", "011", "100", "101", "110", and "111" representing eight units with a phase difference of 45°. The smaller the phase difference of the unit structure of the encoding metasurface is, the more flexible the beam regulation is, making the phase regulation close to the continuous phase. The proposed encoding metasurface makes metamaterials more informationized and become the carrier of more information. Fig. 1 shows a schematic diagram of a polarimetric insensitive Huygens metasurface.

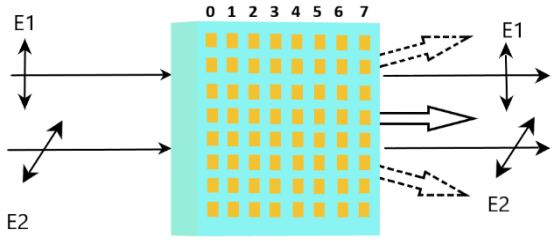

Fig. 1. Schematic diagram of polarimetric insensitive Huygens metasurface (colour online)

In order to achieve polarization insensitivity, we designed the cell structure to be center-symmetric with the same dimensions in the X and Y directions. We adopted three different three-layer structures, as shown in Fig. 2, to achieve 3-bit coding design. The spacing layers of the three different unit structures are the same size and thickness, and only the shape and geometric parameters of the three layers of metal patches are different. The unit structure is composed of two spacer layers and three layers of metal. The spacer layer is a benzocyclobutene (BCB) layer with dielectric constant ε =2.67 and tangential loss of tanδ=0.012. The metal material is gold material. The two spacer layers are square structures with side length a=150μm and thickness d=20μm. The thickness of metal patch is t=0.2μm. The side length of the square metal patch is b, the radius of the circular metal patch is R, the side length of the outer frame of the circular metal patch is X1, and the side length of the inner frame is X2. By scanning parameters b, R, X1, X2 of the element structure of three different metal patches, the phase coverage of 8 element structures is 2π and the phase difference of adjacent element structures is 45°. The specific geometric parameters of the unit structure are shown in Table 1. For easy identification, we coded the 8 cell structures as "0", "1", "2", "3", "4", "5", "6", and "7". Fig. 3 shows the transmission phase and transmission coefficient of the unit structures.

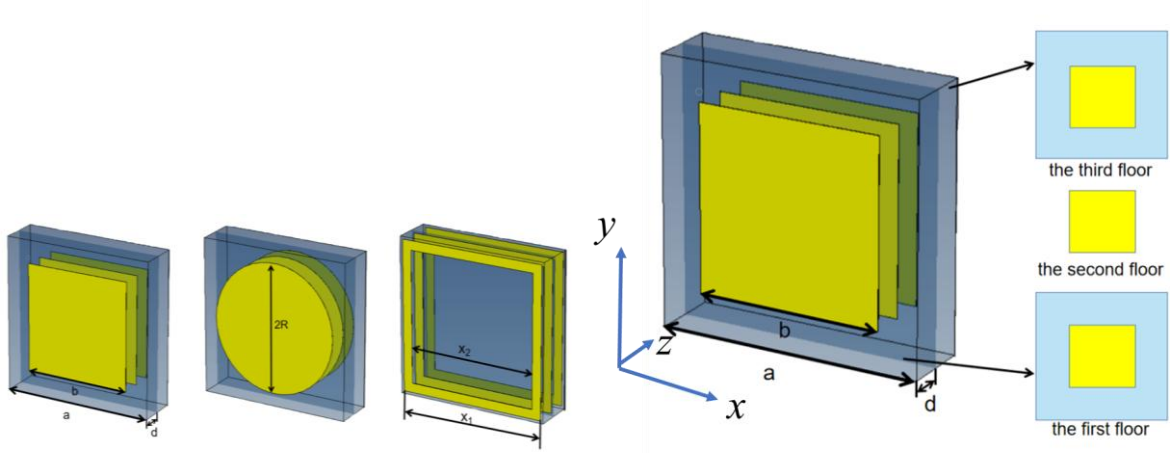

Fig. 2. Schematic diagram of unit structure (colour online)

Table 1. Geometric parameters of unit structures.

Unit Cells								
	"0"	"1"	"2"	"3"	"4"	"5"	"6"	"7"
Parameter Setting /μm	b=105	b=101.6	b=95.45	b=84.6	b=38	X_1=150 X_2=149	X_1=145 X_2=127	R=62.76
Phase (actual value) /°	-75.23	-30.18	15.24	60.38	105.53	150.25	-165.01	-120.87
Phase (theoretical value) /°	-75.23	-30.23	14.77	59.77	104.77	149.77	-165.23	-120.23

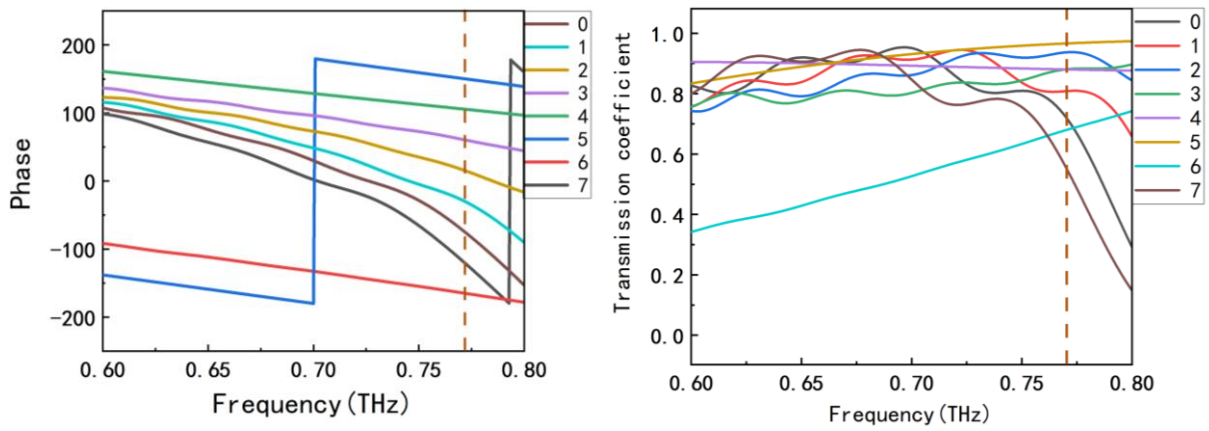

(a) *(b)*

Fig. 3. Transmission phase (a) and transmission coefficient (b) of cell structures (colour online)

Next, we calculated the effective parameters of the cell structures. The S parameter of the element structure is obtained by the solver and the equivalent parameter is calculated by the S parameter inversion algorithm. By using

the S-parameter inversion algorithm, we can obtain the equivalent dielectric constant ε, equivalent permeability μ, impedance Z and refractive index n of the periodic structure. A unit structure with a square patch and a side length of 38μm is taken as an example, and the S-parameter inversion algorithm is combined as [8]

$$n = cos^{-1}[(1 - S_{11}^2 + S_{21}^2)/2S_{21}]/kd \quad (1)$$

$$Z = \{[(1 + S_{11})^2 - S_{21}^2]/[(1 - S_{11})^2 + S_{21}^2]\}^{1/2} \quad (2)$$

$$\mu = nZ,\ \varepsilon = n/Z \quad (3)$$

where n is the refractive index of the equivalent medium, Z is the equivalent impedance, S11 is the reflection coefficient, S21 is the transmission coefficient, k is the incident wave vector, and d is the thickness of the metassurface. The equivalent parameters obtained are shown in Fig. 4, where black represents the real part (Re) and red represents the imaginary part (Im). The dielectric constant ε is shown in Fig. 4 (a), and the real and imaginary parts are symmetric with respect to the horizontal axis. In the range of 0.6 to 1.0THz frequency, the absolute value of permittivity is close to 0, and the bound charge capacity is small. In the range of 1.2THz frequency, the absolute value of permittivity is close to 60, and the bound charge capacity is large. The equivalent permeability μ is shown in Fig. 4 (b). Near the frequencies of 0.6 and 1.0THz, the absolute values of the imaginary and real parts of the permeability of the unit structure reach the peak. In the band of 0.65-0.95THz, the permeability is relatively stable, and the real part remains around 20, and the imaginary part is 0. The trend of the equivalent impedance Z is basically the same as that of the equivalent permeability. The equivalent impedance has a peak near the frequencies 0.6 and 1.0THz, and a relatively stable impedance value of approximately 2.5 is found in the band 0.65-0.95THz. The refractive index of the equivalent medium is shown in Fig. 4 (d). The actual part values are all above 6.0, and the imaginary part values are within the range of 0-1. By calculating the equivalent parameters of these cell structures, we can gain a deeper understanding of the physical properties of the amplitude and phase variations of cell structures.

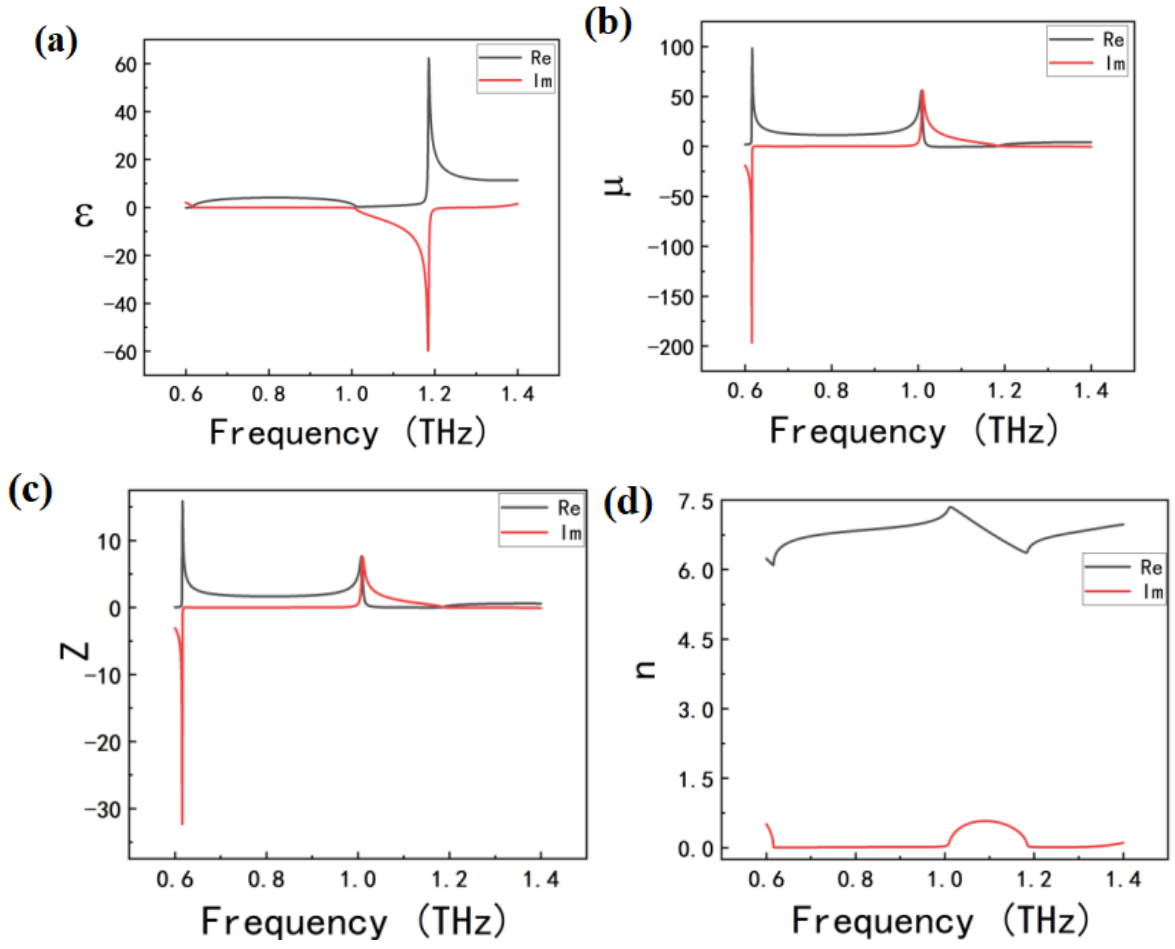

Fig. 4. b=3 8 unit structure equivalent parameters (a) dielectric constant (b) permeability (c) impedance (d) refractive index (colour online)

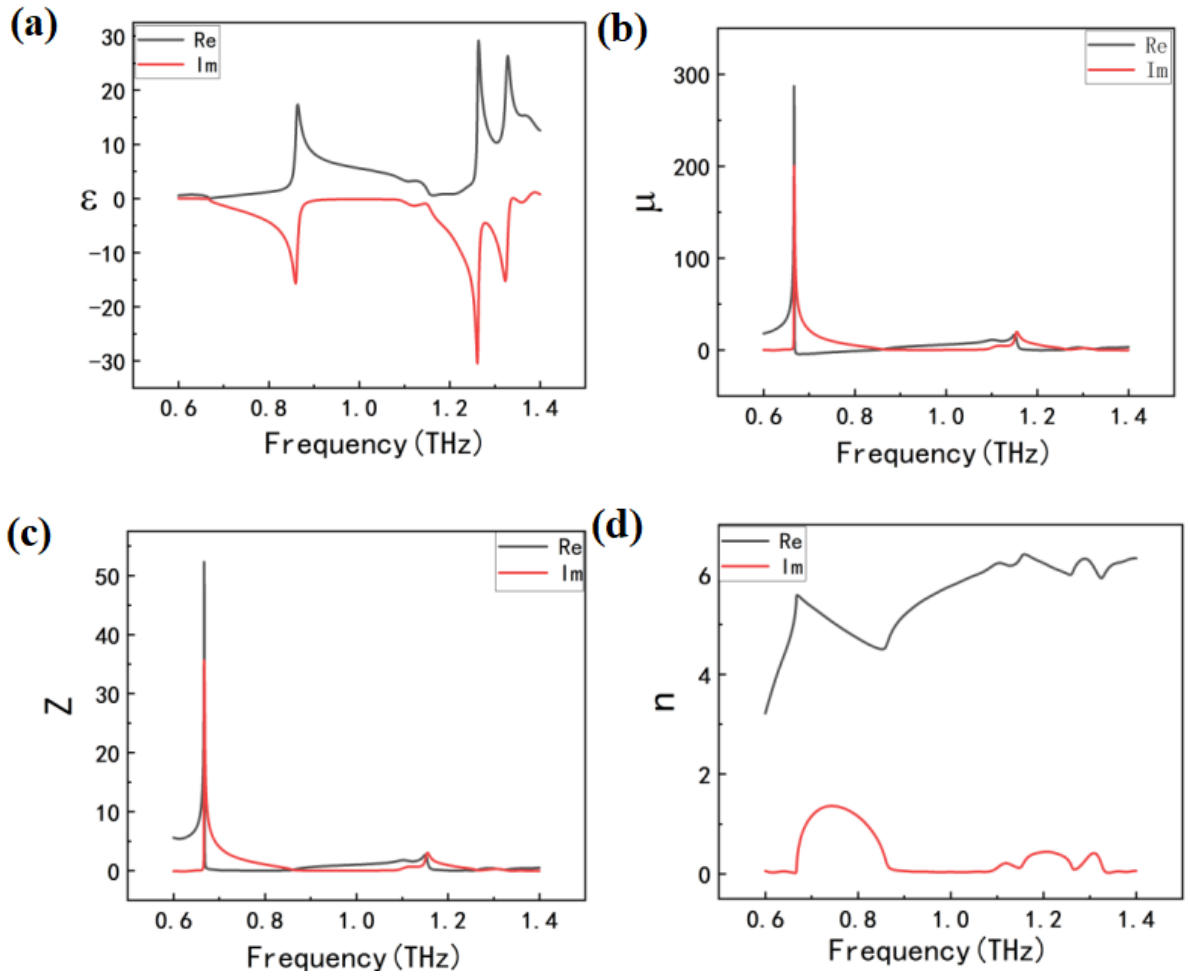

Fig. 5. X1=145, X2=127 unit structure (a) dielectric constant (b) permeability (c) impedance (d) refractive index (colour online)

Fig. 5 shows the equivalent parameter of the elliptical structure, and the dielectric constant is shown in Fig. 5 (a). The real part and the imaginary part are symmetric about the horizontal axis. The absolute value of dielectric constant is close to 0 in the frequency 0.6 to 0.8THz, indicating that the electron binding ability is weak in this band. The absolute value of dielectric constant at the frequencies of 0.83THz, 1.24THz and 1.35THz is larger than that of other bands, so the band has strong electron binding ability.

As shown in Fig. 5(b), the absolute value of the equivalent permeability reaches the peak value near the frequency of 0.68 and 1.18THz, while the absolute value of the equivalent permeability is close to 0 in other bands. The characteristic curves of equivalent impedance and equivalent permeability are similar, and the absolute values reach the peak value near 0.68 and 1.18THz, while the real and imaginary parts of other bands are relatively stable, and the absolute values tend to 0. The refractive index of the equivalent medium is shown in Fig. 5 (d), where the real part is above 3 and the imaginary part is above 0.

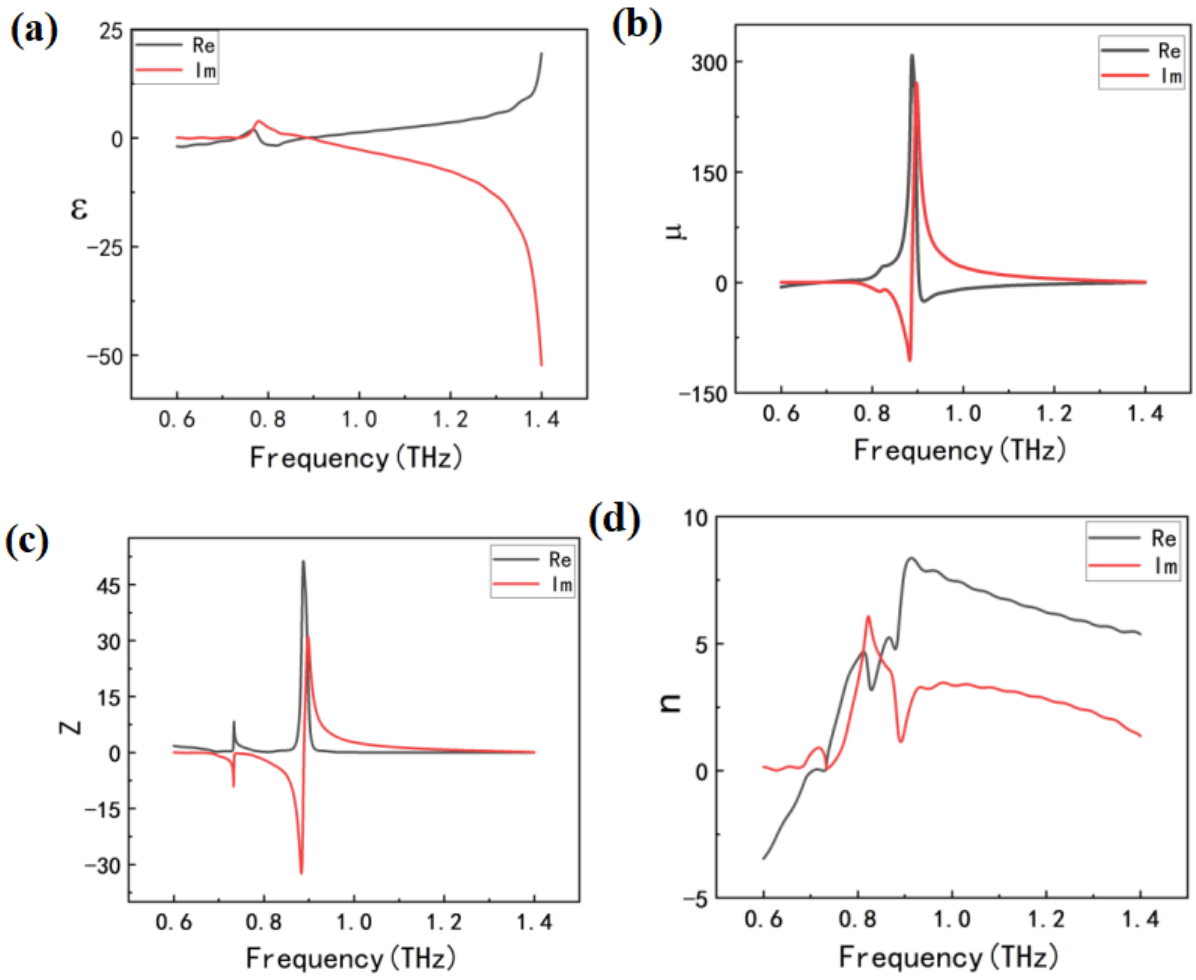

Fig. 6. R=62.76 unit structure (a) dielectric constant (b) permeability (c) impedance (d) refractive index (colour online)

Fig. 6 shows the equivalent parameters of the circular structure. The absolute value of the dielectric constant approaches 0 in the band 0.6 to 1.0THz, and the binding charge ability is weak. The absolute value of dielectric constant increases gradually from 1.0 to 1.4THz, indicating that the capacity of bound charge increases with the increase of frequency. The absolute value of the equivalent permeability is greater than 0 at 0.82 to 1.0THz band, and reaches the peak value at 0.9THz, while the absolute value of the permeability of the other bands approaches 0. The absolute value of the equivalent impedance reaches its peak in the vicinity of 0.7 and 0.9THz bands, while the absolute value of the impedance in other bands is close to 0. The refractive index is shown in Fig. 6 (d). It can be found that the refractive index law of the circular structure is different from that of the circular structure and the square structure. The absolute value of the real part of the refractive index is in the range of 0 to 6, and the absolute value of the imaginary part is in the range of 0 to 5.

The equivalent parameters of other cell structures at the center frequency of 0.77THz are shown in Table 2. From the perspective of equivalent permittivity, the unit structures encoded as "4" and "5" have greater binding charge capacity than other unit structures. The cell structure encoded "4" has the greatest equivalent permeability at the center frequency. From the point of view of the equivalent impedance, the impedance coded "1" is the largest, and the equivalent impedance coded "6" is the smallest. From the perspective of equivalent refractive index, the absolute refractive index values of the unit structures encoded as "1" and "2" are less than 1, while the other unit structures are greater than 1. The combination of impedance Z and refractive index n can be considered as non-zero refractive index metamaterials.

Table 2. The equivalent parameter of the eight-cell structure at the center frequency

Unit cells		“0”	“1”	“2”	“3”	“4”	“5”	“6”	“7”
ε	*Re*	1.293	0.075	-0.541	-0.888	4.036	7.542	0.946	1.674
	Im	0.789	0.060	0.015	-0.08	-0.015	-0.380	-3.231	3.071
μ	*Re*	2.683	1.775	-0.277	-2.687	11.495	4.179	-1.786	3.189
	Im	0.020	0.246	0.190	0.100	0.083	0.280	7.370	-1.180
Z	*Re*	1.282	4.139	0.756	1.739	1.687	0.743	0.035	0.745
	Im	-0.355	-1.139	-0.223	-0.040	0.009	0.043	1.500	-0.644
n	*Re*	1.939	0.383	0.383	-1.545	6.812	5.624	4.881	3.229
	Im	0.553	0.165	0.165	0.021	0.011	0.046	1.305	1.210

3. Phase gradient Huygens coded metasurface

Firstly, the 8-unit structures are coded. The above 8-unit structures are numbered by "0, 1, 2, 3, 4, 5, 6, 7" respectively. The 8 structures are arranged in a counterclockwise direction according to the phase, "0" represents the phase of 0 (360) degrees, "1" represents the phase of 45 degrees, and "2" represents the phase of 90 degrees. "3" represents phase at 135 degrees, "4" represents phase at 180 degrees, "5" represents phase at 225 degrees, "6" represents phase at 270 degrees, and "7" represents phase at 315 degrees. Fig. 7 shows the unit structure constructing the coded metasurface in a phase gradient arrangement with phase increments of 45°. The cell structure is similar to the binary encoding, "0" represents "000", "1" represents "001", "2" represents "010", "3" represents "011", "4" represents "100", "5" represents "101", "6" represents "110" and "7" represents "111". The phase difference of the 8 cell structures is 45°. The size of the encoding metassurface is 12×12 encoding particles, and the Y-axis direction is 1×12 identical unit structure. For the X-axis encoding, S1=0123456701234567, S2=0011223344556677 and other encoding modes can be adopted.

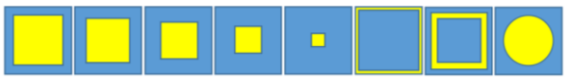

Fig. 7. The coded metasurface was constructed in a phase gradient arrangement with phase increments of 45° C (colour online)

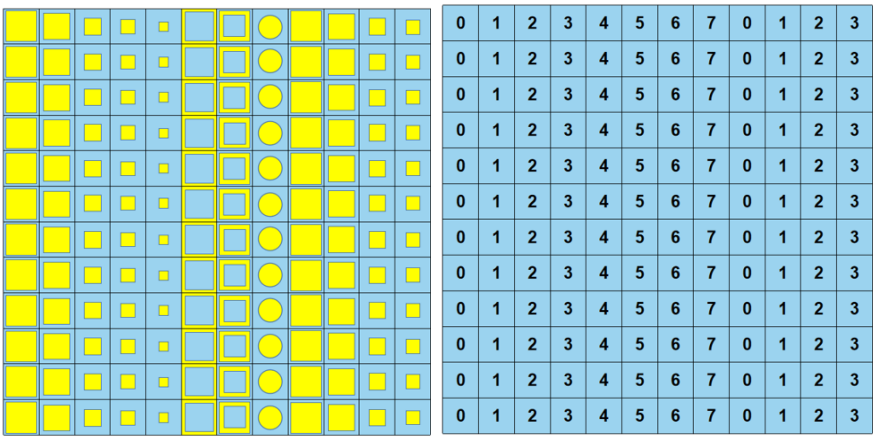

Fig. 8. The coded metasurface diagram with sequence coding S1, (a) is the actual structure diagram of the coded metasurface, and (b) is the digital diagram of the coded metasurface (colour online)

Fig. 8 shows the coded metasurface with sequence encoding S1. Its three-dimensional far-field diagram is shown in Fig. 9 (a) and far-field angle diagram is shown in Fig. 9 (b). The period of S1 is 1200μm. The theoretical value of the abnormal transmission angle θ=18.89° can be obtained by generalized Snell theorem, and the actual value

of the abnormal transmission angle in far-field simulation is θ'=18°. The error of numerical simulation value and theoretical value is within the acceptable range. We can further calculate the near-field electric field diagram and near-field phase diagram of the encoding sequence S1. It is shown in Fig.10. From the near-field electric field diagram of the near-field monitoring plane y=0, it can be seen that the incident light is parallel to the Z axis, and the outgoing light is deflected from the positive semi-axis of Z at a certain angle.

The actual deflection angle is 17.85°, and both errors are within a reasonable range. In the near-field phase diagram, it can be seen that the color distribution in the phase diagram covers all colors from 0 to 360 degrees, so it can be proved that the eight-unit structures cover the phase 2π in a certain order. In the near field phase diagram, it can be seen that the phase of the eight-unit structures increases counterclockwise on the coded metasurface. The incident light perpendicular to the metasurface deflects when exiting, and the deflection angle is consistent with the theoretical value.

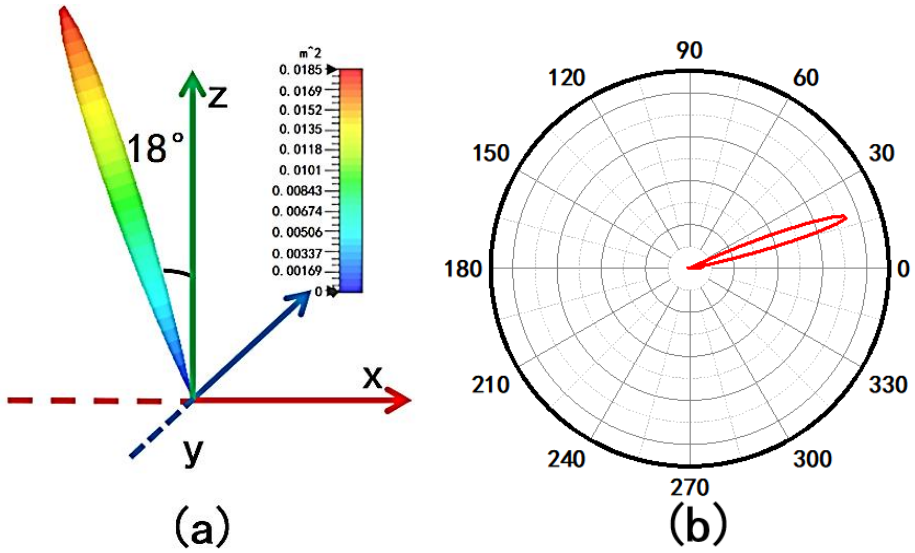

Fig. 9. Diagram of far field scattering angle, (a) diagram of 3D far field, (b) diagram of far field angle (colour online)

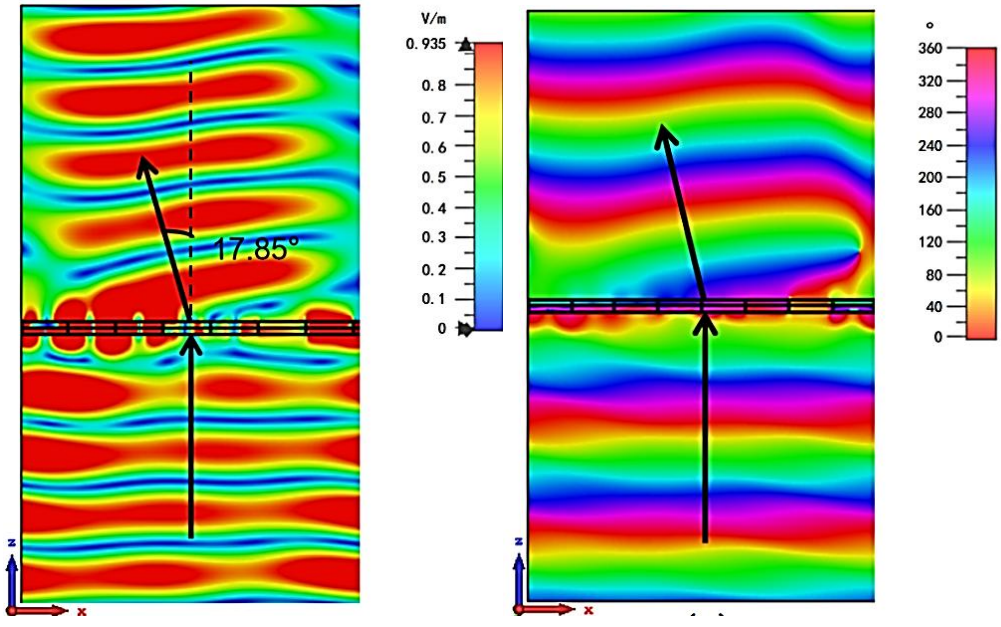

Fig. 10. Encoding metasurface near-field electric field and near-field phase distribution, (a) near-field electric field, (b) near-field phase (colour online)

We calculated the energy distribution of the encoding metasurface in each diffraction order, and the results are shown in Fig. 11. Fig. 11 (a) is the diffraction order of TM incident light, and Fig. 11 (b) is the diffraction order of TE light. The general energy distribution trend of the two cases is similar. The energy in the diffraction direction is basically the same in the TM mode and the TE mode. Therefore, not only the unit structure is polarization-insensitive, but also the coded metasurface composed of 8-unit structures arranged in sequence according to the phase is polarization-insensitive. At the central frequency of 0.772THZ, the energy of diffraction order T+1 is the highest, and up to 65% of the incident energy deflects the diffraction order T+1 with the diffraction angle of 17.85°. Other diffraction signals are weaker.

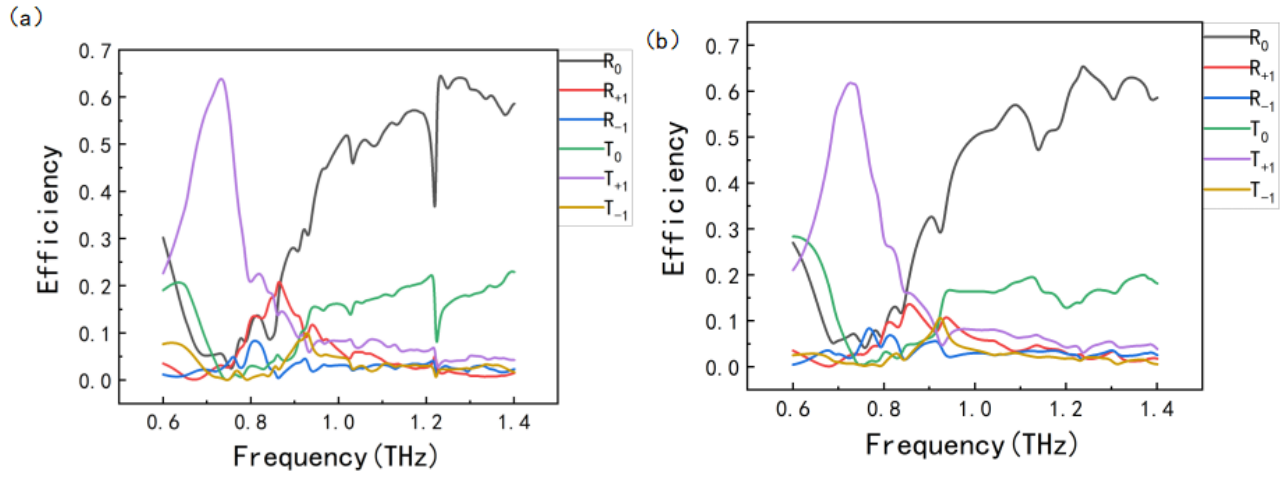

Fig. 11. The energy distribution characteristics of the coded metasurface diffraction order, (a) is the diffraction order in TM mode, (b) is the diffraction order in TE mode (colour online)

4. Fourier convolution operation for encoding Huygens metasurface

Based on the principle of coded metasurface far-field scattered beam and generalized Snell theorem, we can realize the regulation of far-field scattered beam, but the regulation is discrete. Every time the far-field scattering angle is changed, the sequence of metasurface needs to be re-encoded, and the generalized Snell theorem is used to recalculate the angle. The efficiency of such regulation method is too low. Therefore, Fourier convolution principle in digital signal processing is introduced to continuously regulate the far field scattering angle. The electric field of the near field of the metasurface is regarded as the time domain signal, and the scattering of the far field is regarded as the frequency domain signal. Therefore, the electric field of the near field and the scattering of the far field can be regarded as a Fourier transform pair. According to the generalized Snell theorem, both the scattering angle of the far field and the abnormal refraction angle of the near field are related to the period length of the encoding sequence. Changing the period length of the sequence can change the scattering angle of the far field and also change the abnormal refraction angle of the near field electric field. So, we can change the far field scattering angle by changing the abnormal refraction angle of the near field electric field. We can change the signal in the time domain, and the Fourier transform principle is expressed as [60]

$$F(\omega) = \int_{-\infty}^{\infty} f(t) e^{-i\omega t}\, dt \tag{4}$$

We can equivalent the time domain parameter t to the electrical length x_λ of the coded metasurface. Electrical length x_λ is related to the incident light wavelength and super surface sequence cycles. ω can be viewed as the far field scattering angle of relevant variables, and $F(\omega) = F(\sin\theta)$. Changing the abnormal refraction angle of near-field electric field can be realized by time shift in time domain, which can be obtained by Fourier transform and time shift property as0

$$f(t) \cdot e^{j\omega_0 t} \rightarrow F(\omega) * \delta(\omega - \omega_0) = F(\omega - \omega_0) \tag{5}$$

It can be further obtained as

$$f(x_\lambda) \cdot e^{jx_\lambda \sin\theta_0} \rightarrow F(\sin\theta) * \delta\left(\sin\theta - \sin\theta_0\right) = F\left(\sin\theta - \sin\theta_0\right) \tag{6}$$

We can be understood as a move in time domain for $e^{jx_\lambda \sin\theta_0}$, and the spectrum shifts to the right in the frequency domain as $\sin\theta_0$. The properties after the time shift are different from the properties before the time shift,

so it can be considered that the period of the encoding sequence changes in the metasurface, and a new periodic sequence is obtained. The far field scattering angle corresponding to the periodic sequence represented by $f(x_\lambda)\cdot e^{jx_\lambda \sin\theta_0}$ is $sin^{-1}(sin\,\theta - sin\,\theta_0)$. Similarly, if the spectrum shifts to the left, a new coding sequence $f(x_\lambda)\cdot e^{-jx_\lambda \sin\theta_0}$can be obtained, and the corresponding scattering angle is $sin^{-1}(sin\,\theta + sin\,\theta_0)$. We can use the generalized Snell theorem to first calculate the far-field scattering angles of several sequences, and then take these sequences as the basic coding by Fourier convolution principle to obtain new coding sequences, so as to realize the continuous regulation of far-field scattering angles, improve the design efficiency and expand the application field.

By using the principle of Fourier convolution addition, we design the 3-bit coded metasurface. 3-bit one-dimensional coding means that 8 unit structures are encoded in the X-axis, and the Y-axis direction is the same unit structure. The metasurface size is designed for 16×16 encoded particles. The code along the X axis could be S1=0123456701234567... S2=0011223344556677... , S3=00011122233344 4... and a variety of coding methods to meet the requirements. We add the Fourier convolution with S1 and S2 as the base coding sequence. The period of S1 is 8a=1200μm, and the period of S2 is 16a=2400μm. From the generalized Snell's law, it can be obtained as $\theta_1 = sin^{-1}(\lambda/\Gamma) = sin^{-1}(\lambda/8a)$ and $\theta_2 = sin^{-1}(\lambda/\Gamma) = sin^{-1}(\lambda/16a)$. The theoretical abnormal transmission angle $\theta_1 = 18.89°$ for S1 encoding and $\theta_2 = 9.31°$ for S2 encoding. In the actual simulation, the angle corresponding to the code S1 is 20°, and the actual angle corresponding to S2 is 10°. The error between the theoretical value and the simulated value is within the normal range. Therefore, we take S1 and S2 as the basic sequence for Fourier convolution addition calculation to achieve the change of far field scattering angle. The code addition method is 0+0=0, 0+1=1, 1+1= 2, 2 +2= 4, 3 +3= 6, 3 +4= 7, 3 +5=0. Fig. 12 shows the metasurface encoding configuration characteristics of the encoding addition operation and the corresponding far-field scattering characteristics. After Fourier convolution addition operation, S3 sequence is 0134671245702356.... S3=S1+S2. The far-field scattering angle corresponding to S3 can be obtained by using generalized Snell's law as $\theta_3 = sin^{-1}(sin\,\theta_1 + sin\,\theta_2) = sin^{-1}(sin\,18.89 + sin\,9.31) = 29.04°$. Based on far-field scattering simulation, as shown in Fig. 12 (b), the scattering angle value of S3 is 29°, which indicates that there is little error between simulated value and theoretical value.

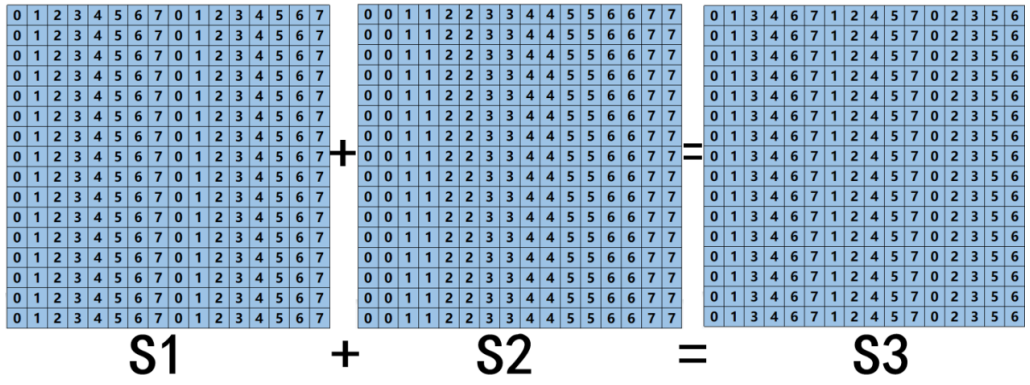

(a)

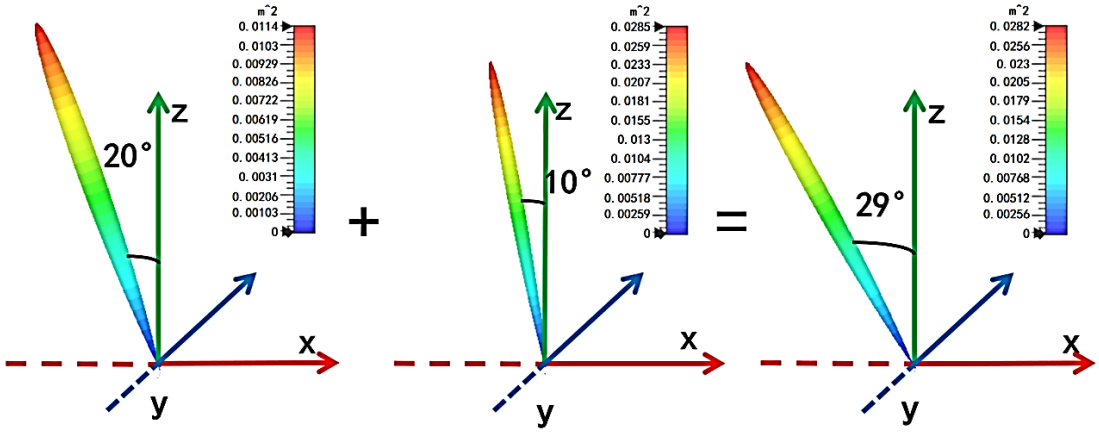

(b)

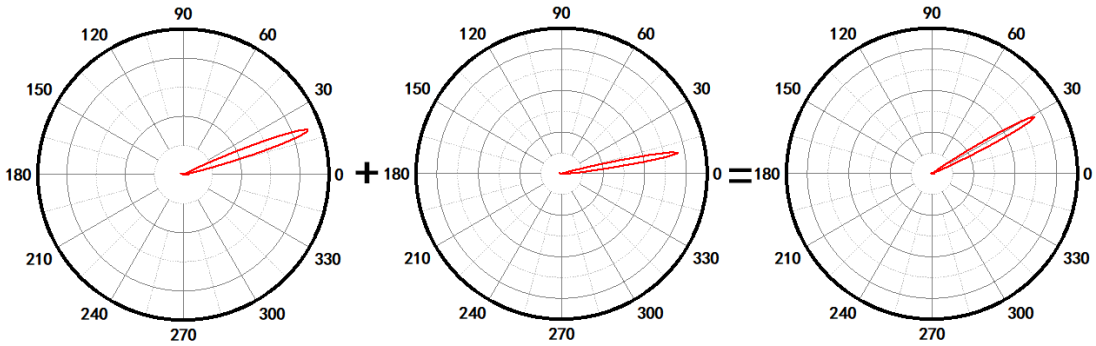

(c)

Fig. 12. The sequence S1 and S2 are added by Fourier convolution to obtain the sequence S3. (a) coding sequence, (b) far field 3D diagram, (c) far field scattering angle (colour online)

We can also use the basic sequence S1 and S2 for subtraction calculation. The encoding calculation method is similar to the binary subtraction method. Subtracting a number is equal to adding the number's complement. In 3-bit, 0 and 7 complement each other, 1 and 6 complement each other, 2 and 5 complement each other, and 3 and 4 complement each other. So, we can get 0-0=0+7=7, 1-5=1+2= 3,3 -4=3+3=6 and so on. Fig. 13 shows the metasurface encoding configuration characteristics of the encoding subtraction operation and the corresponding far-field scattering characteristics. The sequence S4=7001122334455667... can be obtained. And S4=S1-S2. From the Fourier convolution principle we know that Fourier subtraction and Fourier addition are frequency shifts in opposite directions in the frequency domain so we can get the encoded metasface anomalous scattering angle of the Fourier subtraction of S1 and S2 as $\theta_4 = sin^{-1}(sin\,\theta_1 - sin\,\theta_2) = sin^{-1}(sin\,18.89 - sin\,9.31) = 9.32°$. The actual simulated value is 10°, which is in good agreement with the theoretical value.

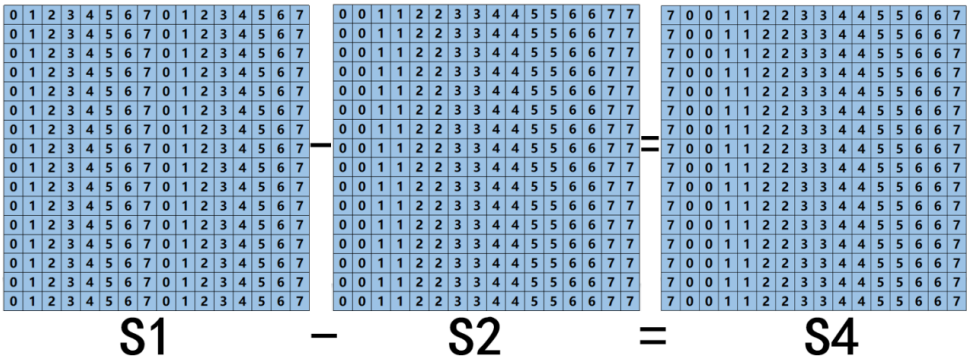

(a)

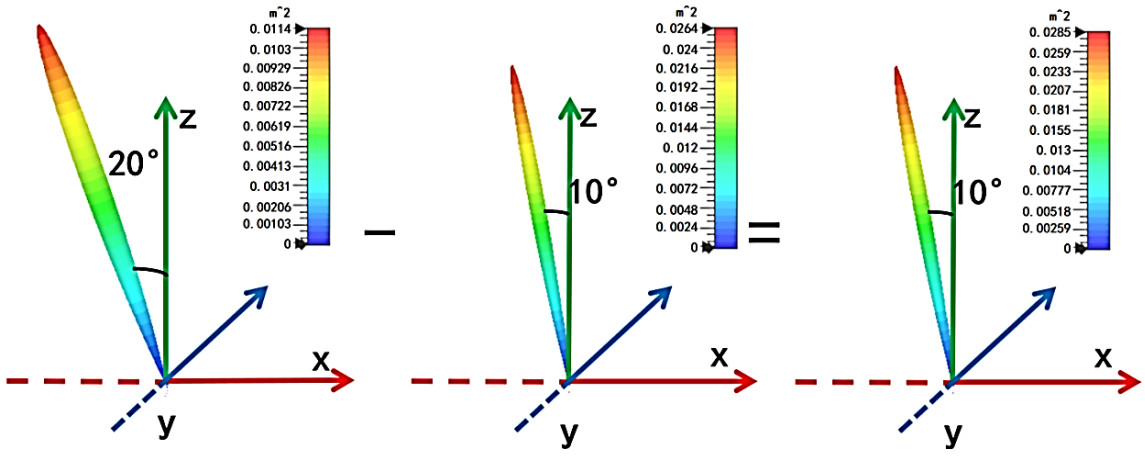

(b)

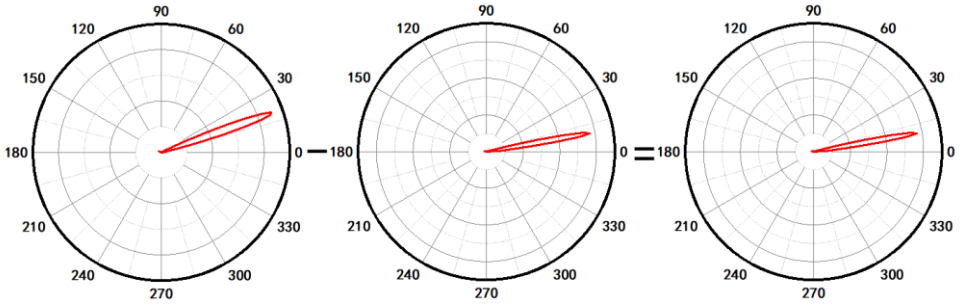

(c)

Fig. 13. The sequence S1 and S2 are subtracted by Fourier convolution to obtain the sequence S4. (a) coding sequence, (b) far field 3D diagram, (c) far field scattering angle (colour online)

Based on the basic sequences S1 and S2, the new sequences S3 and S4 are obtained by Fourier convolution phase addition and subtraction. These two new sequences can also be added or subtracted by Fourier convolution as S3+S4=S5 and S3-S4=S6. Fig. 14 shows the metasurface encoding configuration characteristics of the encoding addition operation and the corresponding far-field scattering characteristics. Fig. 15 shows the metasurface encoding configuration characteristics of the encoding subtraction operation and the corresponding far-field scattering characteristics. The theoretical scattering angles of sequences S5 and S6 are respectively calculated from generalized Snell's theorem as $\theta_5 = sin^{-1}(sin\,\theta_3 + sin\,\theta_4) = sin^{-1}(sin\,29.04 + sin\,9.32) = 40.34°$ and $\theta_6 = sin^{-1}(sin\,\theta_3 - sin\,\theta_4) = sin^{-1}(sin\,29.04 - sin\,9.32) = 18.87°$. The corresponding numerical simulation values were 39° and 19°, respectively, with an error of 0.03 and 0.006. The scattering angles calculated theoretically are in general agreement with the numerical simulations. Through the above simulation results, we can find that the polarization insensitive structure can be in good accordance with the Fourier convolution principle and the far-field scattering principle, and can use the Fourier convolution principle to flexibly and continuously regulate the abnormal refractive angle.

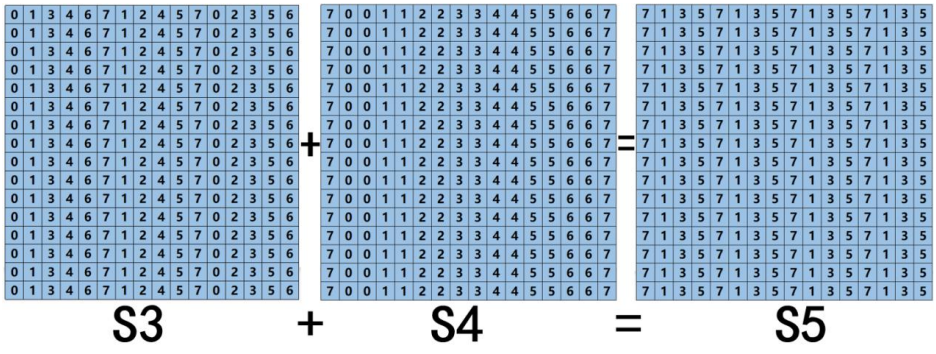

(a)

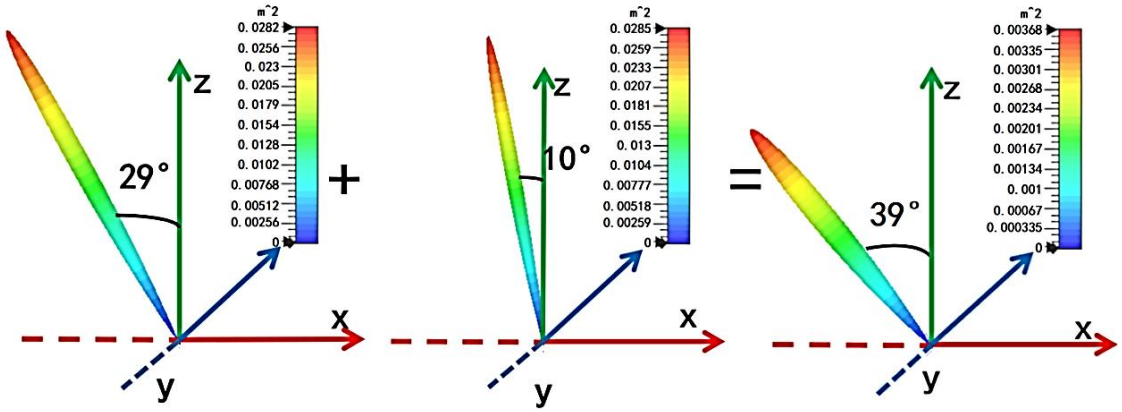

(b)

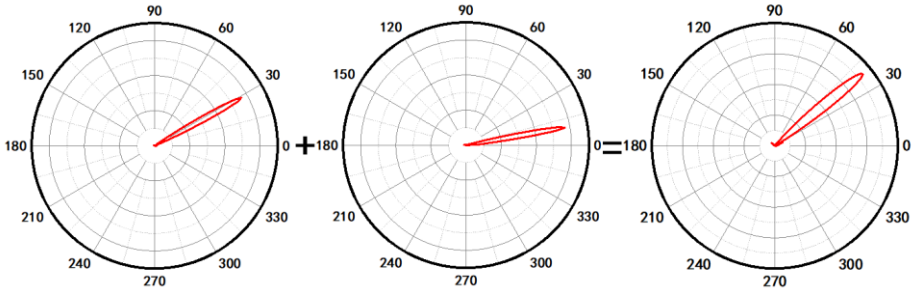

(c)

Fig. 14. The sequence S3 and S4 are added by Fourier convolution to obtain the sequence S5. (a) coding sequence, (b) far field 3D diagram, (c) far field scattering angle (colour online)

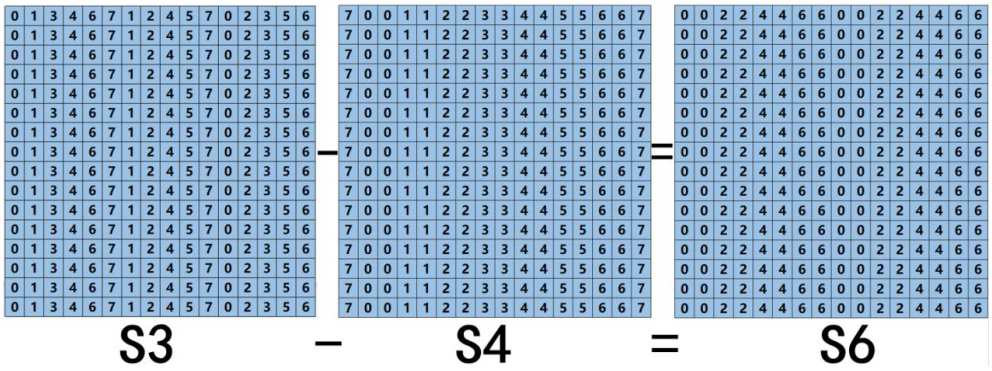

(a)

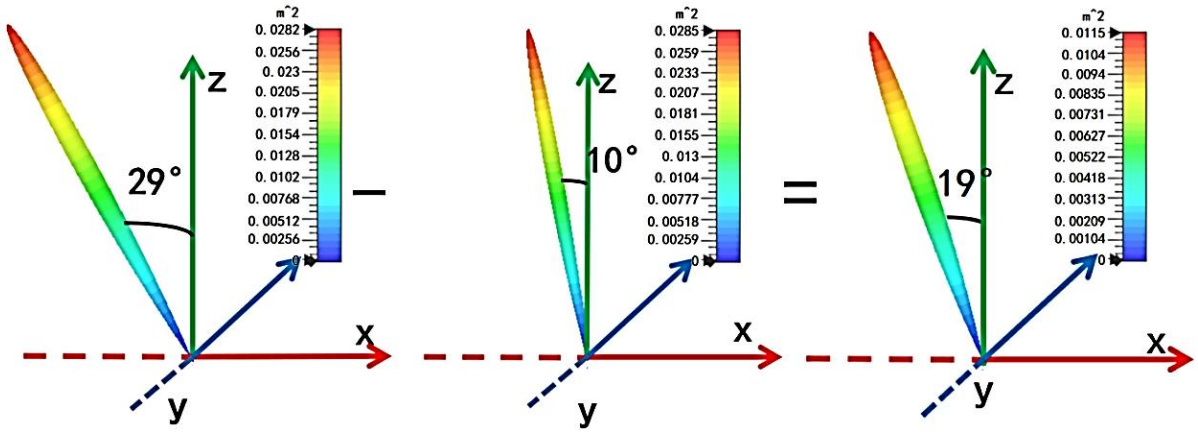

(b)

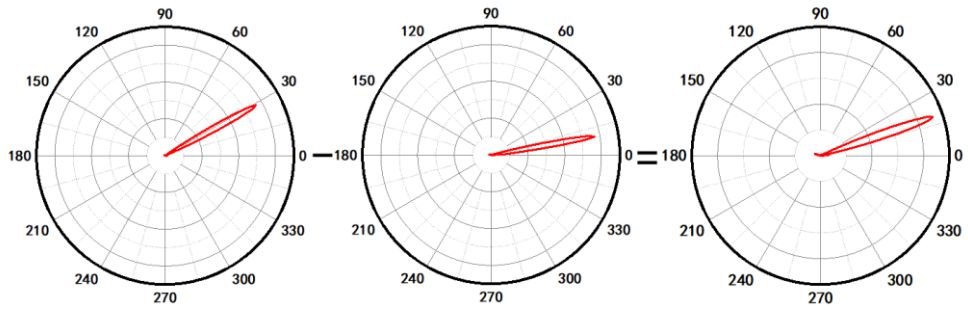

(c)

Fig. 15. The sequence S3 and S4 are subtracted by Fourier convolution to obtain the sequence S6. (a) coding sequence, (b) far field 3D diagram, (c) far field scattering angle (colour online)

5. The checkerboard encodes the Huygens metasurface

The checkerboard code is a two-dimensional encoding metasurface of a 1-bit metasurface, and its cell structure is a cell structure with phase difference of 180° encoding "0" and "1" respectively. The above results show that the sequence coding in a single direction can only produce a single beam, and the checkerboard distribution can be regarded as two complementary sequences. The modulus of "010101..." is the same in the X and Y directions on the basis of the polarization insensitive metasurface. The theoretical formula for the far-field scattering deflection angle of the checkerboard coding distribution is $\theta = sin^{-1}(\sqrt{2}\lambda/\Gamma)$. Fig. 16 (a) shows the arrangement of the checkerboard encoded metasurface and Fig. 16 (b) shows the corresponding far-field 3D scattering. As shown in the figure, we can see that the beam incident from the negative half axis of Z passes through the metasurface and the transmitted beam in the plane xoy along the positive half axis of Z is evenly divided into four beams with basically the same size and energy. In the plane xoy, the beam is symmetric about the Z axis and the angle between each beam and the Z axis is equal. The Z axis can be regarded as the normal line of the plane where the transmitted beam is located. In the 45° azimuth plane, we can see that each beam has an angle of 33° with the positive half axis of Z.

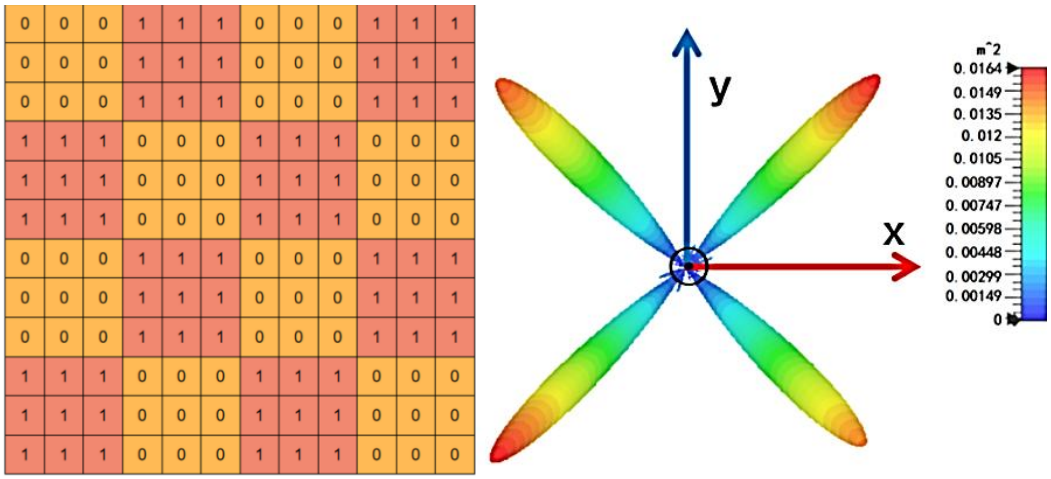

(a) *(b)*

Fig. 16. The checkerboard encodes the metasurface. (a) Schematic representation of the encoded metasurface sequence, and (b) 3D representation of the checkerboard encoded far-field (colour online)

Based on the above metasurface coding and far-field scattering modulation, we perform Fourier convolution operations on the checkerboard coded beam. The metasurface has a 12×12 encoded particle structure. Select "1" and "5" with phase difference of 180° as "0" and "1" in 1-bit coding in 8-cell structure from "0" to "7". The convolution added to the checkerboard coded metasurface is the sequence S= "012345670123..." along the X-axis. The convolution addition operation is shown in Fig. 17. The far field 3D scattering of checkerboard coded metasurface and one-dimensional coded metasurface convolution is shown in Fig. 18. From the convolution results, we can see that the transmitted beam deflects counterclockwise as a whole, and the normal line of the checkerboard coded beam is the Z-axis. When it convolves with the one-dimensional coded metassurface encoded as S, its normal line deflects. The angle between the checkerboard encoded normal and Z positive axis is 0°, the angle between the deflection angle encoded S and Z positive axis is 18°, and the angle between the convolution beam normal and Z axis is 17.76°. The angle of normal rotation is consistent with the angle between the S-coded metasurface beam and the Z axis. After the Fourier convolution addition of checkerboard coded metasurface and one-dimensional coded metasurface, the normal line of the far-field beam generated by checkerboard coded is rotated, and the angle between the normal line and the z-axis is the angle between the far-field scattered beam and the z-axis of the one-dimensional coded metasurface.

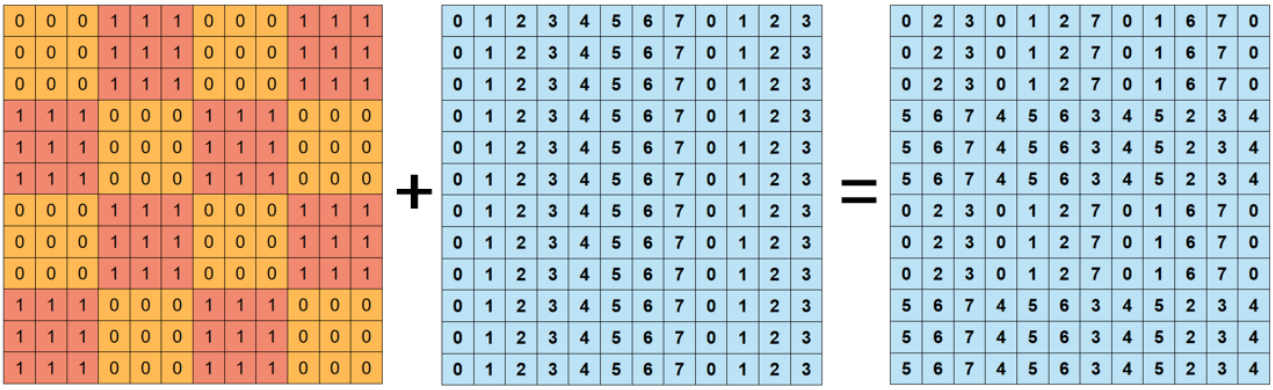

Fig. 17. Chessboard coded metasurface and one-dimensional coded metasurface convolution additive sequence diagram (colour online)

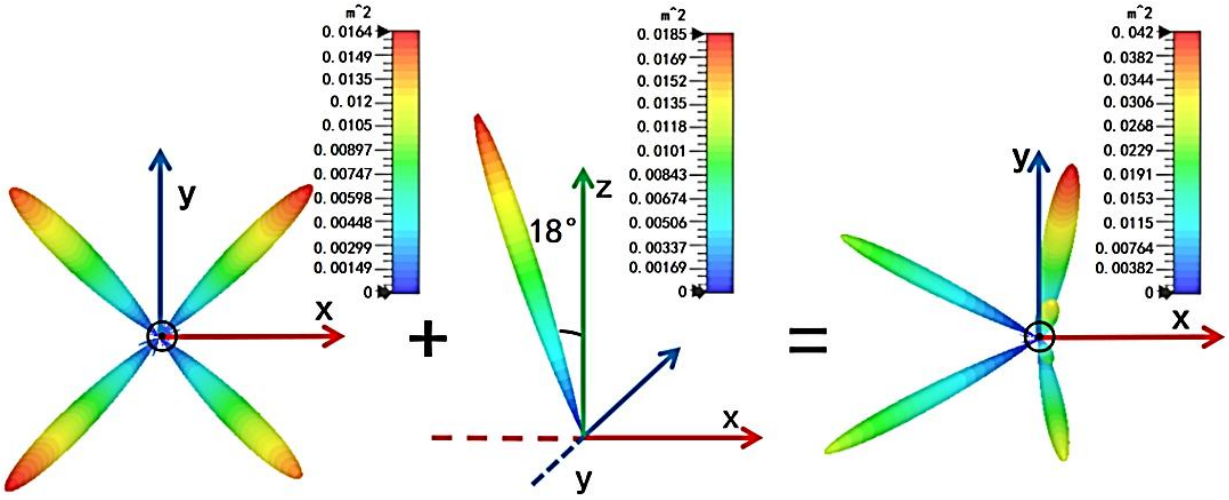

Fig. 18. Far-field 3D scattering map of checkerboard coded metasurface and one-dimensional coded metasurface convolution (colour online)

Although the results of numerical simulation are presented in this paper, the preparation of the three-layer high-efficiency transmissible metasurfaces proposed by us can also be realized [80]. The preparation process mainly includes the traditional photolithography and the preparation of metal films. Firstly, a thick metal layer can be manufactured by using the electron beam evaporation method on silicon wafer. Then, a polyimide layer is spun onto the metal layer and baked on a hot plate. The spinning and baking processes can be repeated twice to produce a thicker polyimide layer. Next, the standard lithography processes can be implemented. The final single metal structure can be obtained through a liftoff process. Finally, the metal pattern and polyimide layers can be separated from the silicon substrate, and the monolayer metasurface structures can be obtained. The above process can be repeated to obtain the other two layers of metasurface structures. The experimental bonding method can be used to obtain the three-layer transmissible metasurface structure. In order to measure the scattering characteristics of the prepared samples, the far-field in-plane scanning measurement with a rotary terahertz time domain system (THz-TDS) can be performed. The fiber-based terahertz photoconductive antennas can be used to generate and receive the terahertz signals in time domain. The optical stabilization platform and the rotary stage should be used for the transmitter and the receiver. In the measurement, the receiver can be rotated in the horizontal plane to record the electric fields scattered from the samples. With the progress of artificial intelligence and computer technology [81-88], the design of the structure we proposed will use advanced artificial intelligence methods, making the structure design more applicable [89-94].

5. Conclusions

We designed a polarization-insensitive three-layer metallic element structure. In order to ensure the transmission characteristics of the unit structure, the metal patches of three different structures were optimized to form eight-unit structures with the best transmission coefficient

and phase difference of 45°. On the basis of these eight elements, they are arranged in order of phase increase to form a phase gradient metasurface. The near field phase, near field electric field, diffraction order and far field scattering angle of the coded metasurface are analyzed. Based on the Fourier convolution principle and the generalized Snell theorem, the Fourier convolution addition and subtraction operations can obtain scattering angles that can be continuously regulated. Based on the far-field scattering angle regulation principle, the cell structure is checkerboard coded, and the checkerboard coding and one-dimensional coding are convolved to obtain the regulation characteristics of multi-beam deflection.

References

[1] X. He, Carbon **82**, 229 (2015).
[2] X. He, X. Zhong, F. Lin, W. Shi, Opt. Mater. Express **6**, 331 (2016).
[3] Xiaoyong He, Feng Liu, Fangting Lin, Wangzhou Shi, Opt. Lett. **46**, 472 (2021).
[4] Xiaoyong He, Feng Liu, Fangting Lin, Wangzhou Shi, J. Phys. D: Appl. Phys. **54**, 235103 (2021).
[5] Jun Peng, Xiaoyong He, Chenyuyi Shi, Jin Leng, Fangting Lin, Feng Liu, Hao Zhang, Wangzhou Shi, Physica E **124**, 114309 (2020).
[6] X. Jing, S. Jin, Y. Tian, P. Liang, Q. Dong, L. Wang, Optics and Laser Technology **48**, 160 (2013).
[7] X. Jing, Y. Xu, H. Gan, Y. He, Z. Hong, IEEE Access **7**, 144945 (2019).
[8] L. Jiang, B. Fang, Z. Yan, J. Fan, C. Qi, J. Liu, Y. He, C. Li, X. Jing, H. Gan, Z. Hong, Optics and Laser Technology **123**, 105949 (2020).
[9] H. Lv, X. Lu, Y. Han, Z. Mou, S. Teng, Optics Letters **44**(10), 2518 (2019).
[10] H. Wang, L. Liu, C. Zhou, J. Xu, M. Zhang, S. Teng, Y. Cai, Nanophotonics **8**(2), 317 (2019).
[11] Linda Shao, Jin Zhang, Ivan D. Rukhlenko, Weiren Zhu, Chin. Opt. Lett. **20**, 103601 (2022).
[12] S. Teng, Q. Zhang, H. Wang, L. Liu, H. Lv, Photonics Research **7**(3), 246 (2019).
[13] M. R. Akram, G. Ding, K. Chen, Y. Feng, W. Zhu, Advanced Materials **32**, 1907308 (2020).
[14] J. Zhang, X. Wei, I. D. Rukhlenko, H.-T. Chen, W. Zhu, ACS Photonics **7**(1), 265 (2020).
[15] Ziyu Liu, Limei Qi, Feng Lan, Chuwen Lan, Jun Yang, Xiang Tao, Chin. Opt. Lett. **20**, 013602 (2022).
[16] Bo Fang, Zhiyu Cai, Yandong Peng, Chenxia Li, Zhi Hong, Xufeng Jing, Journal of Electromagnetic Waves and Applications **33**(11), 1375 (2019).
[17] B. Fang, B. Li, Y. Peng, C. Li, Z. Hong, X. Jing, Microw. Opt. Technol. Lett. **61**, 2385 (2019).
[18] Weimin Wang, Xufeng Jing, Jingyin Zhao, Yinyan Li, Ying Tian, Optica Applicata **47**(2),183 (2017).
[19] L. Jiang, B. Fang, Z. Yan, C. LI, J. Fu, H. Gan, Z. Hong, X. Jing, Microwave and Optical Technology Letters **62**(6), 2405 (2020).
[20] Shunshuo Cai, Wanhan Hu, Yiman Liu, Juan Ning, Sixuan Feng, Chao Jin, Lingling Huang, Xin Li, Chin. Opt. Lett. **20**, 053601 (2022).
[21] Chunyan Jin, Wei Wu, Lei Cao, Bofeng Gao, Jiaxin Chen, Wei Cai, Mengxin Ren, Jingjun Xu, Chin. Opt. Lett. **20**, 113602 (2022).
[22] Pengfei Wang, Fengyan He, Jianjun Liu, Fangzhou Shu, Bin Fang, Tingting Lang, Xufeng Jing, Zhi Hong, Photon. Res. **10**, 2743 (2022).
[23] Yang Zhu, Binbin Lu, Zhiyuan Fan, Fuyong Yue, Xiaofei Zang, Alexei V. Balakin, Alexander P. Shkurinov, Yiming Zhu, Songlin Zhuang, Photon. Res. **10**, 1517 (2022).
[24] Tina Ebert, René Heber, Torsten Abel, Johannes Bieker, Gabriel Schaumann, Markus Roth, High Power Laser Science and Engineering **9**(2), 02000e24 (2021).
[25] Xinhua Xie, Yunpei Deng, Steven L. Johnson, High Power Laser Science and Engineering **9**(4), 04000e66 (2021).
[26] J. Zhang, H. Zhang, W. Yang, K. Chen, X. Wei, Y. Feng, R. Jin, W. Zhu, Advanced Optical Materials **8**, 2000683 (2020).
[27] X. Bai, F. Kong, Y. Sun, F. Wang, J. Qian, X. Li, A. Cao, C. He, X. Liang, R. Jin, W. Zhu, Advanced Optical Materials **8**, 2000570 (2020).
[28] X. Jing, X. Gui, P. Zhou, Z. Hong, Journal of Lightwave Technology 36(12), 2322 (2018).
[29] R. Xia, X. Jing, X. Gui, Y. Tian, Optical Materials Express **7**(3), 977 (2017).
[30] M. R. Akram, M. Q. Mehmood, X. Bai, R. Jin, M. Premaratne, W. Zhu, Advanced Optical Materials **7**, 1801628 (2019).
[31] M. R. Akram, X. Bai, R. Jin, G. A. E. Vandenbosch, M. Premaratne, W. Zhu, IEEE Transactions on Antennas and Propagation **67**(7), 4650 (2019).
[32] J. Zhao, X. Jing, W. Wang, Y. Tian, D. Zhu, G. Shi, Optics and Laser Technology **95**,56 (2017).
[33] Y. Tian, X. Jing, H. Gan, X. Li, Z. Hong, Front. Phys. **15**, 62502 (2020).
[34] C. Zhou, Z. Mou, R. Bao, Z. Li, S. Teng, Front. Phys. **16**, 33503 (2021).
[35] G. Dai, Front. Phys. **16**, 53301 (2021).
[36] L. Lan, Y. Gao, X. Fan, M. Li, Q. Hao, T. Qiu, Front. Phys. **16**, 43300 (2021).
[37] J. Li, R. Jin, J. Geng, X. Liang, K. Wang, M. Premaratne, W. Zhu, IEEE Transactions on Antennas and Propagation **67**(4), 2442 (2019).
[38] X. Lu, X. Zeng, H. Lv, Y. Han, Z. Mou, C. Liu, S. Wang, S. Teng, Nanotechnology **31**, 135201 (2020).
[39] H. Lv, X. Lu, Y. Han, Z. Mou, C. Zhou, S. Wang, S. Teng, New J. Phys. **21**, 123047 (2019).

[40] B. Fang, D. Feng, P. Chen, L. Shi, J. Cai, J. Li, C. Li, Z. Hong, X. Jing, Front. Phys. **17**, 53502 (2022).
[41] Jitao Li, Guocui Wang, Zhen Yue, Jingyu Liu, Jie Li, Chenglong Zheng, Yating Zhang, Yan Zhang, J. Q. Yao, Opto-Electronic Advances **5**(1), 210062 (2022).
[42] Jitao Li, Jie Li, Chenglong Zheng, Zhen Yue, Silei Wang, Mengyao Li, Hongliang Zhao, Yating Zhang, Jianquan Yao, Carbon **182**, 506 (2021).
[43] Jitao Li, Jie Li, Chenglong Zheng, Silei Wang, Mengyao Li, Hongliang Zhao, Jiahui Li, Yating Zhang, Jianquan Yao, Carbon **172**, 189 (2021).
[44] Jitao Li, Jie Li, Chenglong Zheng, Zhen Yue, Dingyu Yang, Silei Wang, Mengyao Li, Yating Zhang, J. Q. Yao, Applied Physics Letters **119**, 241105 (2021).
[45] Jitao Li, Jie Li, Chenglong Zheng, Chenglong Zheng, Zhen Yue, Silei Wang, Mengyao Li, Hongliang Zhao, Yating Zhang, J. Q. Yao, Physics Letters **118**, 221110 (2021).
[46] H. X. Xu, G. Hu, L. Han, M. Jiang, Y. Huang, Y. Li, X. Yang, X. Ling, I. Chen, J. Zhao, C.-W. Qiu, Advanced Optical Materials **7**(4), 1801479 (2019).
[47] X. Wang, H. X. Xu, Y. Wang, C. Zhang, S. Wang, M. Wang, X. Yang, Advanced Photonics Research **2**(10), 2100102 (2021).
[48] H. X. Xu, Y. Wang, C. Wang, M. Wang, S. Wang, F. Ding, Y. Huang, X. Zhang, H. Liu, X. Ling, W. Huang, Research **2021**, 6382172 (2021).
[49] H. X. Xu, G. Hu, M. Jiang, S. Tang, Y. Wang, C. Wang, Y. Huang, X. Ling, H. Liu, J. Zhaou, Advanced Materials Technologies **5**(1), 1900710 (2020).
[50] H. X. Xu, G. Hu, Y. Li, L. Han, J. Zhao, Y. Sun, F. Yuan, G.-M. Wang, Z. H. Jiang, X. Ling, T. J. Cui, C.-W. Qiu, Light: Science and Applications **8**, 3 (2019).
[51] He-Xiu Xu, Chaohui Wang, Guangwei Hu, Yanzhao Wang, Shiwei Tang, Yongjun Huang, Xiaohui Ling, Wei Huang, Cheng-Wei Qiu, Adv. Opt. Mater. **9**(11), 2100190 (2021).
[52] Jin Leng, Jun Peng, An Jin, Duo Cao, Dejun Liu, Xiaoyong He, Fangting Lin, Feng Liu, Optics and Laser Technology **146**, 107570 (2022).
[53] Xiaoyong He, Feng Liu, Fangting Lin, Wangzhou Shi, Annalen der Physik **534**(4), 2100355 (2022).
[54] Yan Peng, Chenjun Shi, Yiming Zhu, Min Gu, Songlin Zhuang, PhotoniX **1**(1), 12 (2020).
[55] C. J. Shi, X. Wu, Y. Peng, Opto-Electron Eng. **47**(5), 190638 (2020).
[56] Yan Peng, Jieli Huang, Jie Luo, Zhangfan Yang, Liping Wang, Xu Wu, Xiaofei Zang, Chen Yu, Min Gu, Qing Hu, Xicheng Zhang, Yiming Zhu, Songlin Zhuang, PhotoniX **2**, 12 (2021).
[57] Cui, Tie Jun, Mei Qing Qi, Xiang Wan, Jie Zhao, Qiang Cheng, Light: Science and Applications **3**(10), e218 (2014).
[58] S. Liu, T. J. Cui, Q. Xu, D. Bao, L. Du, X. Wan, W. X. Tang, C. Ouyang, X. Y. Zhou, H. Yuan, H. F. Ma, W. X. Jiang, J. Han, W. Zhang, Q. Cheng, Light: Science and Applications **5**(5), e16076 (2016).
[59] Lei Zhang, Xiao Qing Chen, Shuo Liu, Qian Zhang, Jie Zhao, Jun Yan Dai, Guo Dong Bai, Xiang Wan, Qiang Cheng, Giuseppe Castaldi, Vincenzo Galdi, Tie Jun Cui, Nat. Commun. **9**, 4334 (2018).
[60] Shuo Liu, Tie Jun Cui, Lei Zhang, Quan Xu, Qiu Wang, Xiang Wan, Jian Qiang Gu, Wen Xuan Tang, Mei Qing Qi, Jia Guang Han, Wei Li Zhang, Xiao Yang Zhou, Qiang Cheng, Advanced Science **3**, 1600156 (2016).
[61] S. Liu, L. Zhang, G. D. Bai, T. J. Cui, Sci. Rep. **9**, 1809 (2019).
[62] Wenyun Du, Meiping Zhu, Jun Shi, Tianbao Liu, Jian Sun, Kui Yi, Jianda Shao, High Power Laser Science and Engineering **11**(5), 05000e61 (2023).
[63] Bo Bao, Yu Hua, Ridong Wang, Dachao Li, Adv. Quantum Technol. **6**(5), 2200146 (2023).
[64] Jitao Li, Guocui Wang, Zhen Yue, Jingyu Liu, Jie Li, Chenglong Zheng, Yating Zhang, Yan Zhang, Jianquan Yao, Opto-Electron. Adv. **5**(1), 210062 (2022).
[65] H. Zhao, X. K. Wang, S. T. Liu, Y. Zhang, Opto-Electron. Adv. **6**(2), 220012 (2023).
[66] Shilin Liu, Wenhan Cao, Shizeng Jiang, Lianhao He, Fangting Lin, Xiaoyong He, Advanced Quantum Technologies **7**(4), 2300386 (2024).
[67] Dianzhen Cui, Xuexi Yi, Li-Ping Yang, Adv. Quantum Technol. **6**(5), 2300037 (2023).
[68] Sunny Howard, Jannik Esslinger, Robin H. W. Wang, Peter Norreys, Andreas Döpp, High Power Laser Science and Engineering **11**(3), 03000e32 (2023).
[69] Karim Achouri, Ville Tiukuvaara, Olivier J. F. Martin, Advanced Photonics **5**(4), 046001 (2023).
[70] Zeyang Liu, Danyan Wang, Hao Gao, Moxin Li, Huixian Zhou, Cheng Zhang, Advanced Photonics **5**(3), 034001 (2023).
[71] Jiawei Yan, Gianluca Geloni, Advanced Photonics Nexus **2**(3), 036001 (2023).
[72] Nian Zhang, Baoxing Xiong, Xiang Zhang, Xiao Yuan, Advanced Photonics Nexus **2**(3), 036013 (2023).
[73] Quan Xu, Yuanhao Lang, Xiaohan Jiang, Xinyao Yuan, Yuehong Xu, Jianqiang Gu, Zhen Tian, Chunmei Ouyang, Xueqian Zhang, Jiaguang Han, Weili Zhang, Photonics Insights **2**(1), R02 (2023).
[74] Hyunjung Kang, Dohyeon Lee, Younghwan Yang, Dong Kyo Oh, Junhwa Seong, Jaekyung Kim, Nara Jeon, Dohyun Kang, Junsuk Rho, Photonics Insights **2**(2), R04 (2023).
[75] Guoqing Wang, Francesca Madonini, Boning Li, Changhao Li, Jinggang Xiang, Federica Villa, Paola Cappellaro, Adv. Quantum Technol. **6**(9),

2300046 (2023).
[76] Yinhui Kan, Sergey I. Bozhevolnyi, Shailesh Kumar, Adv. Quantum Technol. **6**(12), 2300196 (2023).
[77] Hui Gao, Xuhao Fan, Yuxi Wang, Yuncheng Liu, Xinger Wang, Ke Xu, Leimin Deng, Cheng Zeng, Tingan Li, Jinsong Xia, Wei Xiong, Opto-Electron. Sci. **2**, 220026 (2023).
[78] Yijia Huang, Tianxiao Xiao, Shuai Chen, Zhengwei Xie, Jie Zheng, Jianqi Zhu, Yarong Su, Weidong Chen, Ke Liu, Mingjun Tang, Peter Müller-Buschbaum, Ling Li, Opto-Electron. Adv. **6**, 220073 (2023)
[79] Jia Chen Dapeng Wang, Guangyuan Si, Siew Lang Teo, Qian Wang, Jiao Lin, Opto-Electron. Adv. **6**, 220141 (2023).
[80] X. Jing, Y. Ke, Y. Tian, H. Gan, Y. He, C. Li, Z. Hong, IEEE Access **8**, 164795 (2020).
[81] Z. Zhou, B. Xue, H. Wang, J. Zhao, Multimedia Tools and Applications **83**(9), 27809 (2024).
[82] Z. Sun, J. Zhao, Z. Zhou, Q. Gao, Knowledge-Based Systems **225**, 107115 (2021).
[83] J. Zhao, T. Huang, Z. Zhou, F. Cao, Neurocomputing **372**, 8 (2020).
[84] J. Zhao, Y. X. Lu, Z. Zhou, Computers and Electrical Engineering **86**, 106757 (2020).
[85] J. Zhao, N. Chen, Z. Zhou, Multimedia Tools and Applications **79**, 14103 (2020).
[86] Z. Zhou, W. Zhang, J. Zhao, International Journal of Machine Learning and Cybernetics **10**, 3201 (2019).
[87] J. Zhao, C. Chen, Z. Zhou, F. Cao, Journal of Visual Communication and Image Representation **58**, 651 (2019).
[88] J. Zhao, W. Zhang, F. Cao, Multimedia Tools and Applications **77**, 30969 (2018).
[89] Cade Peters, Andrew Forbes, Adv. Photon. **6**, 040501 (2024).
[90] Jianmei Shi, Chengao Yang, Yihang Chen, Tianfang Wang, Hongguang Yu, Juntian Cao, Zhengqi Geng, Zhiyuan Wang, Haoran Wen, Hao Tan, Yu Zhang, Dongwei Jiang, Donghai Wu, Yingqiang Xu, Haiqiao Ni, Zhichuan Niu, High Power Laser Science and Engineering **12**, 04000e42 (2024).
[91] Joonhyuk Seo, Jaegang Jo, Joohoon Kim, Joonho Kang, Chanik Kang, Seong-Won Moon, Eunji Lee, Jehyeong Hong, Junsuk Rho, Haejun Chung, Adv. Photon. **6**, 066002 (2024).
[92] Zaharit Refaeli, Gilad Marcus, Yariv Shamir, High Power Laser Sci. Eng. **12**, 02000e18 (2024).
[93] H. Yang, H. R. He, Y. Q. Hu, H. Duan, Opto-Electron. Eng. **51**(8), 240168 (2024).
[94] H. X. Wang, Y. L. He, H. W. Zhu, H. Dong, S. Wang, Opto-Electron. Eng. **51**(8), 240095 (2024).

*Corresponding authors: 154495791@qq.com